

Magnetically Programmable Surface Acoustic Wave Filters: Device Concept and Predictive Modeling

Michael K. Steinbauer^{1,2,3,*}, Peter Flauger^{1,2}, Matthias Küß⁴, Stephan Glamsch⁴, Emeline D. S. Nysten⁵, Matthias Weiß⁵, Dieter Suess^{1,2}, Hubert J. Krenner⁵, Manfred Albrecht⁴, and Claas Abert^{1,2}

¹*University of Vienna, Faculty of Physics, Physics of Functional Materials, 1090 Vienna, Austria*

²*University of Vienna, Research Platform MMM Mathematics-Magnetism-Materials, 1090 Vienna, Austria*

³*University of Vienna, Vienna Doctoral School in Physics, 1090 Vienna, Austria*

⁴*University of Augsburg, Institute of Physics, 86135 Augsburg, Germany*

⁵*Universität Münster, Physikalisches Institut, 48149 Münster, Germany*

*Corresponding author; e-mail address: michael.karl.steinbauer@univie.ac.at

(Dated: August 1, 2025)

Filtering surface acoustic wave (SAW) signals of specified frequencies depending on the strength of an external magnetic field in a magnetostrictive material has garnered significant interest due to its potential scientific and industrial applications. Here, we propose a device that achieves selective SAW attenuation by instead programming its internal magnetic state. To this end, we perform micromagnetic simulations for the magnetoelastic interaction of the Rayleigh SAW mode with spin waves (SWs) in exchange-decoupled Co/Ni islets on a piezoelectric LiTaO₃ substrate. Due to the islets exhibiting perpendicular magnetic anisotropy, the stray-field interaction between them leads to a shift in the SW dispersion depending on the magnetic alignment of neighboring islets. This significantly changes the efficiency of the magnetoelastic interaction at specified frequencies. We predict changes in SAW transmission of 28.9 dB/mm at 3.8 GHz depending on the state of the device. For the efficient simulation of the device, we extend a prior energy conservation argument based on analytical solutions of the SW to finite-difference numerical calculations, enabling the modeling of arbitrary magnetization patterns like the proposed islet-based design.

I. INTRODUCTION

Surface acoustic wave (SAW) devices are integral to the modern telecommunications infrastructure, where they have already functioned as high-performance band-pass filters for decades [1–3]. The foundational principle for their application as filters was established with the introduction of specially shaped electrodes, called interdigital transducers (IDTs), on piezoelectric substrates [4].

An alternating voltage applied to a transmitting IDT excites SAWs within the substrate. These waves propagate across the substrate to a receiving IDT, where they are converted back to an electrical signal. The geometric configuration of the IDT dictates the resonance frequency at which SAWs can be excited, along with higher-order harmonics. This inherent frequency selectivity enables the precise bandpass filtering characteristic of SAW devices, while their small size and operating range in the radio frequency (RF) regime make them ideal for use in hand-held devices like smartphones [5, 6].

This basic functionality of SAW devices can be extended by modifying the substrate between the IDTs in various ways, enabling their application as lab-on-a-chip platforms for advancements across diverse disciplines, including physics, chemistry, and medicine [7–10]. A significant area of recent interest involves the interaction of these phononic devices with magnetism, since both can be excited in the RF range [11, 12]. Specifically, the excitation of spin waves (SWs) via the magnetoelastic effect has emerged as a promising tool in magnonics, offering numerous potential applications [13, 14]. One such application is the ability to absorb specific frequencies, de-

pendent on the strength of an applied external magnetic field, when the SAW interacts with a magnetic thin film [15–19].

This can be achieved, because SAW attenuation is only efficient at frequencies where its dispersion relation intersects with that of the SW. There, the SAW's energy is transduced to a SW, where it then dissipates via Gilbert damping [20–22]. The crossover point of the dispersion relations can be precisely tuned by adjusting the strength of an external magnetic field, as the field shifts the SW dispersion relation, thereby repositioning the resonance point to a desired frequency. By tuning this point to the band-pass frequency, signals are attenuated, whereas when detuned, the signal passes without attenuation, resulting in highly efficient signal filtering. However, implementing such a device would necessitate the continuous operation of a variable electromagnet, which is undesirable for many potential applications.

In this study, we propose a different method to deliberately shift the SW dispersion, where we utilize exchange-decoupled, but stray-field interacting, thin magnetic islets with out-of-plane (OOP) magnetization and a large magnetic moment (see Fig. 1). The magnetization direction of each islet, influenced by the device's magnetic history, can align along either the positive or negative z-axis. This orientation significantly alters the SW dispersion relation, which in turn impacts SAW absorption. This inherent variability allows for diverse device configurations to manipulate both the amount of absorption and the frequency band of its occurrence. Once programmed via a variable external magnetic field or spin torque methods, the islets maintain a stable magnetic state, requiring

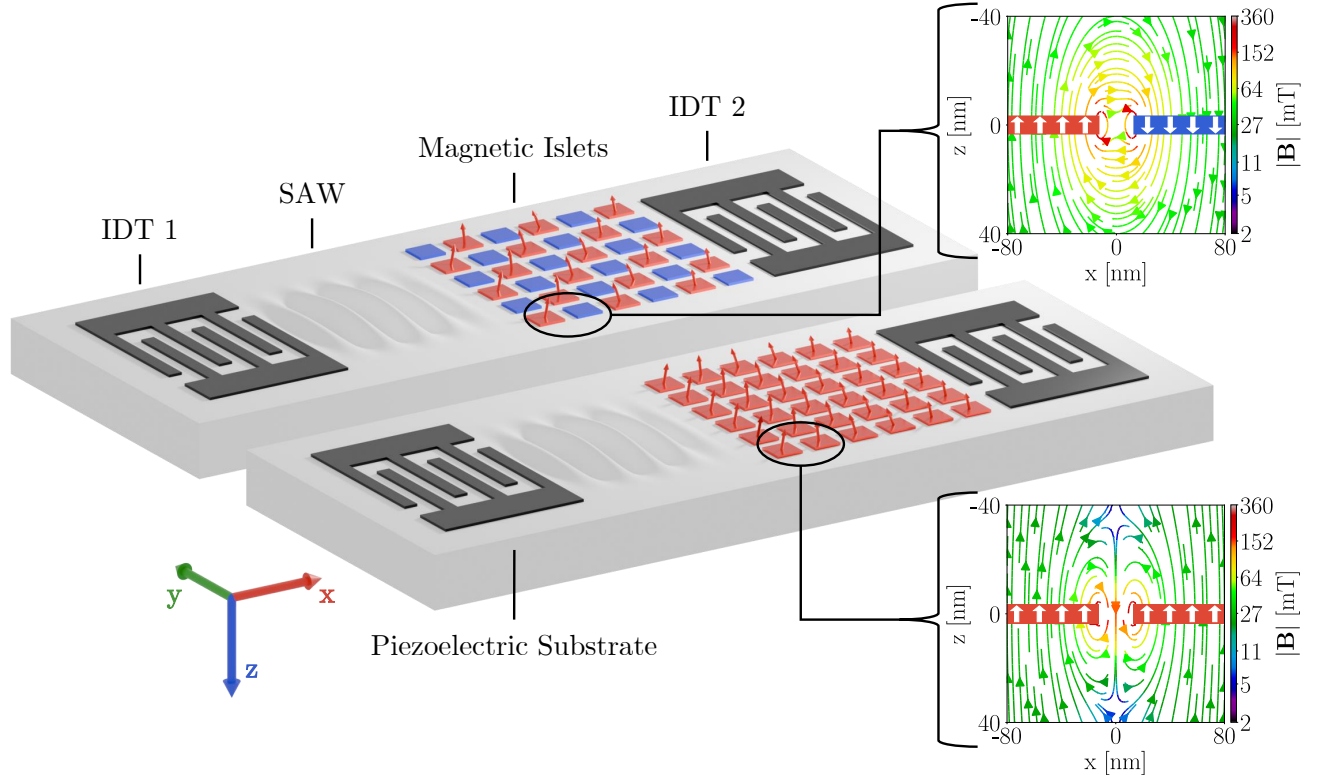


FIG. 1: Illustration of the proposed device in antiparallel configuration (top) and parallel configuration (bottom). In real applications, the islets would be much smaller and more numerous than is suggested here and covered with a capping layer. Insets show cross-sections of the stray-fields between neighboring islets.

only a constant bias field to facilitate magnetoelastic interaction. We compare two device configurations: the A-state, where adjacent islets have antiparallel magnetic moments, and the P-state, where they are parallel. In the A-state, stray fields form flux closures, which enhance the internal magnetic fields within the islets. This increases the system's stiffness and, consequently, its resonance frequencies compared to islets in the P-state, where magnetic field lines repel. Therefore, we anticipate a shift in the SW dispersion relation between the P- and A-states, leading to differences in SAW absorption, which we test using the Rayleigh SAW mode as an example.

II. RESULTS

A. Micromagnetics

In order to explore the feasibility of the proposed device, we make use of micromagnetism, which enables the simulation of spatially varying magnetization patterns, a crucial requirement due to the islet-based architecture of the device. The equation of motion is given by the Landau-Lifshitz-Gilbert equation (LLG) [23, 24]

$$\frac{d\mathbf{m}}{dt} = \frac{-\gamma}{1 + \alpha^2} [\mathbf{m} \times \mathbf{H}_{\text{Eff}} + \alpha \mathbf{m} \times (\mathbf{m} \times \mathbf{H}_{\text{Eff}})], \quad (1)$$

where $\gamma = \mu_0 \gamma_e$ is the reduced gyromagnetic ratio with the vacuum permeability μ_0 , $\mathbf{m} = \mathbf{M}/M_s$ is the reduced magnetization with the saturation magnetization M_s and α is the Gilbert damping. The effective field \mathbf{H}_{Eff} is given by the negative variational derivative of the total magnetic energy E_M with respect to the magnetic polarization. E_M can be comprised of several energy contributions in the magnetic region(s) Ω , such as the Zeeman energy under an external field \mathbf{H}_{ext} , stray-field energy with demagnetization field \mathbf{H}_{dem} , exchange energy with exchange stiffness A_{ex} , and uniaxial magnetic anisotropy with strength K_u along the easy axis \mathbf{e}_u [25]. To describe the interaction of the SAW with the magnetic islets of the device, E_M also has to include a magneto-elastic energy term E_{MagEl} describing the coupling of the normalized magnetization \mathbf{m} with the displacement of the material \mathbf{u} . This term is given by [26–29]

$$E_{\text{MagEl}} = \frac{1}{2} \int_{\Omega} (\boldsymbol{\varepsilon} - \boldsymbol{\varepsilon}_m) : \mathbf{C} : (\boldsymbol{\varepsilon} - \boldsymbol{\varepsilon}_m) \, d\mathbf{x} \quad (2)$$

$$\varepsilon_{ij} = \frac{1}{2} \left(\frac{\partial u_i}{\partial x_j} + \frac{\partial u_j}{\partial x_i} \right) \quad (3)$$

$$\varepsilon_{m,ij} = \begin{cases} \frac{3}{2}\lambda_s(m_i^2 - \frac{1}{3}) & i=j \\ \frac{3}{2}\lambda_s m_i m_j & i \neq j \end{cases} \quad (4)$$

where C is the stiffness tensor, λ_s the saturation magnetostriction, ε the strain associated with the displacement, ε_m the strain associated with the local magnetization and ":" denotes the Frobenius inner product. In Eq. (4), a polycrystalline material with at least cubic symmetry was assumed. E_M and \mathbf{H}_{eff} can then be expressed by

$$E_M = \int_{\Omega} -\mu_0 M_s \mathbf{m} \cdot \left[\mathbf{H}_{\text{Ext}} + \frac{1}{2} \mathbf{H}_{\text{dem}} \right] + A_{\text{ex}} \sum_{i,j} \left(\frac{\partial m_i}{\partial x_j} \right)^2 - K_u (\mathbf{m} \cdot \mathbf{e}_u)^2 + \frac{1}{2} (\varepsilon - \varepsilon_m) : C : (\varepsilon - \varepsilon_m) \, d\mathbf{x} \quad (5)$$

$$\mathbf{H}_{\text{eff}} = - \frac{1}{\mu_0 M_s} \frac{\delta E_M}{\delta \mathbf{m}}. \quad (6)$$

Self-consistent solvers, capable of simulating the coupled magnetic and mechanical dynamics from initial- and boundary conditions of the magnetization, displacement, and momentum can be found in ref. [29] for finite-element models and ref. [30] for finite-difference models. However, these self-consistent approaches are computationally intensive. This is because they need to solve multiple coupled differential equations each timestep. Crucially, they must also simulate large parts or even the entire substrate. Because the substrate is often significantly thicker than the magnetic region, this can increase the system size by multiple orders of magnitude, leading to substantially increased simulation times.

B. Uni-Directional Model

To mitigate this problem and efficiently calculate the magnetic transmission losses ΔS_{ij} of a SAW signal due to interaction with the magnetic islets of the device, we augment the macrospin model developed in ref. [15, 16, 31] with micromagnetic simulations performed with the finite-difference python library magnum.np [32]. These losses in decibels are given by

$$\Delta S_{ij} = 10 \log_{10} \left(\frac{P_{\text{out}}}{P_{\text{in}}} \right), \quad (7)$$

where P_{in} and P_{out} are the SAW power before and after interaction with the device, respectively. Note that ΔS_{ij} only takes into account the magnetoelastic interaction and disregards other contributions to the total transmission losses S_{ij} . In the model, the displacement \mathbf{u} drives magnetization processes as part of the LLG according to Eq. 1-6. However, the back action from this interaction

is assumed to result solely in a decay of the SAW amplitude which gets estimated from an energy conservation argument.

Unlike macrospin-based magneto-acoustic models [15, 16, 31], this approach is capable of predicting the results even for complex magnetization textures like the islet design, as no analytical solutions for the spin wave dynamics have to be provided. Namely, given the parameterization of some SAW mode with velocity c , we simulate the rate of energy transfer from the elastic into the magnetic system, R_T , over a few periods of the SAW until this energy flow becomes constant ($\frac{d}{dt} R_T = 0$). From this value and the total SAW energy E_{Ph} , obtained with a thin-film approximation in a presimulation step, we can estimate the spatial rate for the energy loss of the SAW, allowing us to determine ΔS_{ij} for a signal that has traversed the islet pattern of length l :

$$\Delta S_{ij}(l) = \frac{10}{\ln(10)} \frac{l - R_T}{c E_{\text{Ph}}} \quad (8)$$

$$R_T = - \int_{\Omega} \left(\frac{\partial}{\partial t} \varepsilon \right) : C : \varepsilon_m \, d\mathbf{x} \quad (9)$$

$$E_{\text{Ph}} = \frac{1}{2} \int_V \varepsilon : C : \varepsilon + \rho \mathbf{v}^2 \, d\mathbf{x}. \quad (10)$$

Here, V is the volume of the simulated section, Ω are the magnetic region(s) of that volume, ρ is the material density, and $\mathbf{v} = \frac{du}{dt}$. Because only R_T has to be determined in simulation, but vanishes outside Ω , this reduces the computational complexity from 3D to quasi-2D for thin magnetic structures, like is the case with the islet design, leading to a significant increase in computational speed. A detailed derivation and validation of the model can be found in the Methods section.

C. Material Parameters and Device Geometry

Co/Ni multilayer structures were identified as a possible material candidate for the magnetic islets of the programmable device. They have shown OOP uniaxial magnetic anisotropy, a sizable magnetic moment [33–35], which is necessary in order to maximize the stray-field interaction between the islets themselves, and a moderate Gilbert damping [34, 35]. The parameters used in this section are based on a Ta(3 nm)/Pt(20 nm)/[Co(0.4 nm)/Ni(0.3 nm)]₁₀/Ta(3 nm)/Pt(3 nm) film studied in ref. [33]. While the magnetostriction coefficient λ_s , necessary to facilitate efficient phonon-magnon coupling, was not measured in ref. [33], similar multilayer structures have shown substantial λ_s values [36]. λ_s , as well as other properties not directly available in the literature, were estimated from the individual bulk values of the materials. The parameters used for the simulation of the magnetic Co/Ni multilayer are given in Tab. I [33–35, 37–41], while the parameters for Ta and Pt are taken from

ref. [41–43]. To prevent the islets from coupling via exchange interaction, we separate them with a demagnetized spacer material where $A_{\text{ex}} = \mathbf{m} = K_u = 0$. The mechanical properties of both spacings and islets are approximated to be identical and isotropic.

TABLE I: Assumed material parameters used for the simulation of the magnetic Co/Ni multilayer, based on a Ta(3 nm)/Pt(20 nm)/[Co(0.4 nm)/Ni(0.3 nm)]₁₀/Ta(3 nm)/Pt(3 nm) film. [33–35, 37–41]

A_{ex} [pJ/m]	M_s [kA/m]	K_u [kJ/m ³]	α [1]	λ_s [10 ⁻⁶]	ρ [kg/m ³]	E [GPa]	ν [1]
10	725	366	0.05	-51.71	9141	270.7	0.263

Here, E is the Young modulus and ν the Poisson ratio. The uniaxial magnetic anisotropy K_u along the OOP direction is larger than the thin film shape anisotropy ($\frac{1}{2}\mu_0 M_s^2$) giving rise to an effective OOP easy axis direction.

Each islet has a size of $200 \times 200 \times 36 \text{ nm}^3$ with a spacing of 25 nm between them and is placed on a 36°-rotated Y-cut X-propagation LiTaO₃ substrate. We investigate two distinct configurations of these islets (see Fig. 2): A 1D device designed to characterize the behavior of islets situated atop a waveguide and a 2D device representative of a conventional SAW filter. Due to the increased number of neighbors in the 2D device, we expect the shift in dispersion relation to be more pronounced compared to the 1D case.

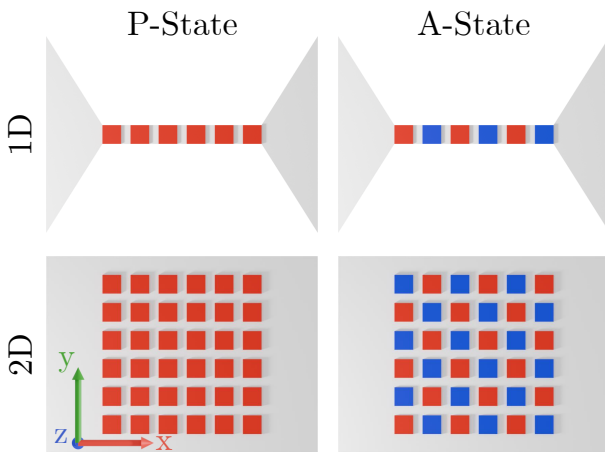


FIG. 2: Illustration of the studied islets in parallel (P) and antiparallel (A) configurations in a 1D and 2D device: Red signifies a magnetization pointing OOP away from the substrate, blue into the substrate.

To model these configurations, islets are arranged in a line and periodic boundary conditions (PBCs) in x direction are applied for the 1D device, whereas for the 2D device, they are arranged in an $n \times 2$ grid with PBCs in

both the x and y directions. The application of PBCs is essential for accurate device modeling, as it mitigates finite-size effects of the stray field, thereby enabling the simulation of the whole device from a much smaller sub-region. For both devices, the discretization of the simulation geometry is (5 nm, 5 nm, $\frac{7}{4}$ nm) when simulating magnetization dynamics, where only the 7 nm thick Co/Ni multilayer is considered. During calculation of E_{Ph} , where the entire layer stack and the substrate are included, the discretization in the z direction is reduced to 1 nm.

D. Dispersion Relation

In order to investigate the programmability of the proposed device, we calculate the spin wave dispersion for the parallel and antiparallel state, employing the methodology proposed in ref. [44], where a magnetic sinc-pulse $\mathbf{h}_{\text{excite}}$ in space and time is used to excite all possible SW modes at once. In addition, the OOP uniaxial magnetic anisotropy K_u , a constant bias field $\mu_0 H_{\text{ext}} = 50 \text{ mT}$ applied along the x-axis and the demagnetization and exchange energies are considered. The external field will later be necessary to facilitate the magneto-phononic interaction and shift the dispersion relation of the spin wave into a desired frequency range. It could be provided by a bias magnet in an experimental realization.

The 1D and 2D magnetic islet patterns are 24 islets long (5.4 μm) in this simulation. After initial relaxation using a Gilbert damping α of 1 and without $\mathbf{h}_{\text{excite}}$, the simulation is performed for 20 ns with 1 ps integration steps and $\alpha = 10^{-8}$. The Gilbert damping was set close to zero in order to sharpen the dispersion relation. During this, the magnetization gets saved for each time step, from which the dispersion relation gets calculated via a Fast Fourier Transform. The simulation results are presented in Fig. 3: The islet pattern magnonic crystal [45] shows a complicated discretized dispersion relation which largely differs for the P- and A-state. As expected, the shift for the 2D device (1.25 GHz) is larger than that of the 1D device (0.3 GHz).

E. SAW parameterization

While LiTaO₃ can support both shear horizontal and Rayleigh SAW modes [46], this study will focus on the Rayleigh mode. Because this mode exhibits non-vanishing displacement both in the direction of travel and transversal to it [47], it has a sense of rotation, leading to a non-reciprocal absorption of the SAW depending on the direction of travel under an external field [16, 21]. This non-reciprocity will be used to validate the uni-directional model in the methods section.

Using the convention of a z-axis which starts at the surface and points into the device, a parameterization of the Rayleigh mode is given in ref. [48] as:

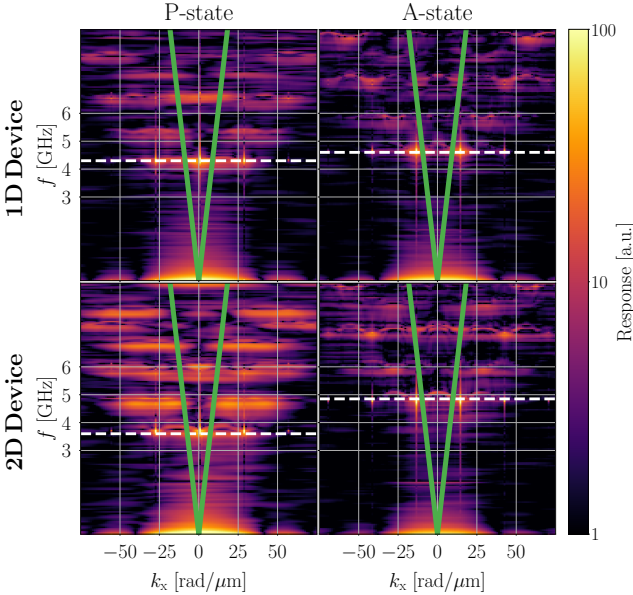


FIG. 3: Magnetization dynamics response of the 1D and 2D devices in the P- and A-states to a magnetic sinc pulse under the influence of a 50 mT bias field along the x direction. The scales of the plot were limited to the range of 1 to 100 to emphasize the relevant data. The linear SAW dispersion relation for $c = 3104.5 \text{ m/s}$ is overlaid as a solid green line.

Maximum responses in the 3 GHz to 6 GHz range are highlighted by white dashed lines: 4.30 GHz and 4.60 GHz for the P and A-states, respectively, of the 1D device; 3.60 GHz and 4.85 GHz for the 2D device.

$$\mathbf{u} = A \frac{\tilde{\mathbf{u}}}{\max(|\tilde{\mathbf{u}}|)} \quad (11)$$

$$\tilde{u}_x(x, z, t) = \kappa_t \cos(kx - \omega t) \cdot \left[\exp(-\kappa_t z) - \frac{2k^2}{k^2 + \kappa_t^2} \exp(-\kappa_l z) \right] \quad (12)$$

$$\tilde{u}_y(x, z, t) = 0 \quad (13)$$

$$\tilde{u}_z(x, z, t) = -k \sin(kx - \omega t) \cdot \left[\exp(-\kappa_t z) - \frac{2\kappa_t \kappa_l}{k^2 + \kappa_t^2} \exp(-\kappa_l z) \right] \quad (14)$$

where A is the amplitude of the SAW, with κ_l and κ_t being the longitudinal- and transversal penetration components. They depend on the angular frequency ω and wave number k of the SAW, as well as the longitudinal- and transversal velocities v_l and v_t :

$$\kappa_l = \sqrt{k^2 - \frac{\omega^2}{v_l^2}} \quad (15)$$

$$\kappa_t = \sqrt{k^2 - \frac{\omega^2}{v_t^2}}. \quad (16)$$

These equations were derived for a single homogeneous material. However, we assume they still model the full device well, because the islets' thickness of 36 nm is significantly lower than the employed SAW wavelengths ($\approx 0.5 \mu\text{m}$ to $1.0 \mu\text{m}$), resulting in the majority of the SAW energy being confined to the substrate rather than the islets. The dispersion relation is then given by [49]

$$\omega = v_t \xi k, \quad (17)$$

where we identify $v_t \xi$ to be the velocity c of the SAW with ξ being the positive, real valued solution of the governing equation [49]

$$\xi^6 - 8\xi^4 + 8\xi^2 \left(3 - 2 \frac{v_t^2}{v_l^2} \right) - 16 \left(1 - \frac{v_t^2}{v_l^2} \right) = 0. \quad (18)$$

To determine v_t and v_l , a finite-element simulation of the substrate was carried out using COMSOL® [50] at $f = 4.47 \text{ GHz}$ where the resulting depth profile of $\mathbf{u}(\mathbf{x}, t)$ was fitted to Eq. 12 and 14. $\mathbf{u}(\mathbf{x}, t)$ is thus parametrized by the values in Tab. II for Eq. 11 to 18, where A_0 was chosen such that it is large enough to minimize numerical errors, while also being small enough to stay in the linear regime of the LLG.

TABLE II: SAW parameters

c [m/s]	v_l [m/s]	v_t [m/s]	A_0 [pm]
3104.5	5586.8	3404.8	4.00

F. Magneto-Phononic Interaction

To calculate the SAW transmission of our devices, we sequentially excite them with SAWs between 3 GHz and 6 GHz. The frequencies used, f_{SAW} , were chosen such that n of their corresponding wavelengths are equal to $2m$ islets and spacings, where n and m are integers:

$$n \frac{c}{f_{\text{SAW}}} = 2m \cdot (200 \text{ nm} + 25 \text{ nm}). \quad (19)$$

This is necessary to ensure that PBCs can be used. The simulated section of the magnetic pattern then consists of $2m$ islets and buffers. Note that this section can be much smaller than the total length of the islet pattern ($\approx 1 \text{ mm}$). For each design, configuration, and frequency, the following procedure was then repeated: During the calculation of E_{Ph} with Eq. 10, the islets were placed upon the LiTaO₃ substrate with ≈ 3 wavelengths thickness, which is thick enough to capture almost all of the total SAW energy. The density of the substrate was taken to be 7450 kg/m^3 [41, 51] and its stiffness matrix was approximated as isotropic and calculated with $C_{11} = \rho v_l^2$, $C_{44} = \rho v_t^2$ [49].

The initial magnetization configuration of the islets was set along the OOP axis and neighboring islets are initialized either with parallel or antiparallel magnetization, depending on the state of the device, after which this state was relaxed at $\alpha = 1$ under the influence of (i) demagnetization energy, (ii) exchange energy with stiffness A_{ex} , (iii) OOP uniaxial anisotropy with strength K_u and (iv) Zeeman energy of a 50 mT external field along the x-axis. For the simulations themselves, $\alpha = 0.05$ was set and the (v) magneto-elastic energy with saturation magnetization λ_s was added to energy terms (i) to (iv). Then, the SAW was activated and the simulation proceeded with a time discretization of $\Delta t = \frac{1}{50f_{\text{SAW}}}$. At each time step, ΔS_{21} was calculated according to Eq. 8 for a 1 mm long islet pattern. The simulation concludes when, for 50 consecutive time steps (one period of the SAW), the relative change in ΔS_{21} is less than 10^{-5} or its absolute change is less than 10^{-3} dB:

$$\left| \frac{\Delta S_{21}(t) - \Delta S_{21}(t - \Delta t)}{\Delta S_{21}(t)} \right| < 10^{-5} \quad (20)$$

$$|\Delta S_{21}(t) - \Delta S_{21}(t - \Delta t)| < 10^{-3} \text{ dB}. \quad (21)$$

This convergence criterion, while equivalent to requiring a constant energy flow because $\Delta S_{21} \propto R_T$, is better suited for practical applications. The final ΔS_{21} value is then determined by averaging ΔS_{21} over these 50 time steps to further mitigate numerical noise.

In the simulated section of the magnetic pattern (with a length of $2m$ islets and buffers), we set $A(x) = A_0 = \text{const}$. This is necessary, because it allows the use of PBCs. Nevertheless, this introduces a small error to the calculation, because the SAW attenuation in this small section slightly changes $\frac{\partial u}{\partial x}$ and thus ϵ . However, this error is negligible when the decay of $A(x)$ within one wavelength of the SAW is small, as is the case there. The transmission efficiency itself is independent of the choice of A , as only the ratio between R_T and E_{Ph} is relevant for its calculation (Eq. 8) and both are proportional to A^2 in the linear regime of the LLG.

At $f_{\text{SAW}} = 4.599$ GHz, where the SAW wavelength is an integer multiple of the periodicity of the islets ($\lambda = \frac{3104.5 \text{ m/s}}{4.599 \text{ GHz}} = 3.225 \text{ nm}$), conditions from Eqs. (20) or (21) were not met within 10ns of simulation time for any device or configuration. Similarly, for $f_{\text{SAW}} = 3.449$ GHz, where $\lambda = \frac{3104.5 \text{ m/s}}{3.449 \text{ GHz}} = 4 \cdot 225 \text{ nm}$, the A-state of the 1D device did not converge (the other three simulations at that frequency did, however). For all five of these simulations, the instantaneous ΔS_{21} values oscillated slightly (< 0.3 dB at 4.599 GHz and ≈ 1.8 dB at 3.449 GHz) around a constant value, where that value would be consistent with those of the surrounding frequencies. These simulations were nevertheless not included in the results.

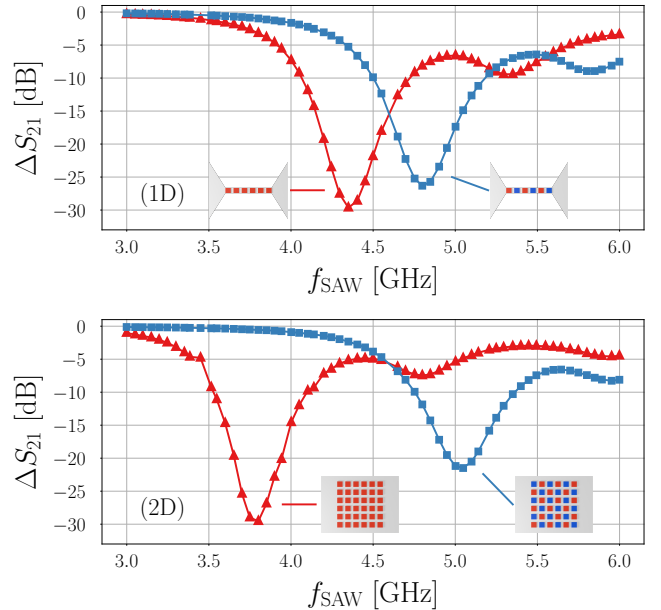


FIG. 4: Simulation results for the transmission losses due to the magnon-phonon interaction, ΔS_{21} , after 1 mm travel distance in the 1D (top) and 2D (bottom) devices at different frequencies of the SAW in different magnetic states: parallel (red triangles) and antiparallel (blue squares). Insets show illustrations of the different islet arrangements. Simulations were performed under the influence of a 50 mT bias field along the x direction.

G. Interpretation

Figure 4 shows the transmission losses ΔS_{21} of the SAW resulting from magnon-phonon interaction in both 1D and 2D devices, under parallel and antiparallel configurations. A notable shift in the location of the transmission dips is observed in the 1D and 2D devices (0.45 GHz and 1.25 GHz, respectively), which largely correlates with the SW resonance modes presented in Fig. 3, albeit at slightly higher frequencies than predicted. This deviation is attributed to the broad spectral response observed from the sinc pulse excitation. The smaller transmission dips appearing at higher frequencies (e.g. 4.80 GHz and 5.95 GHz for the 2D P-state) are also in agreement with the detected SW modes between 3 GHz and 6 GHz in Fig. 3. Importantly, significant differences in SAW attenuation between the states are observed, which is optimized for our 2D device at 3.80 GHz, with $\Delta S_{21} = -29.5$ dB/mm in the P-state and only -0.6 dB/mm in the A-state.

While the presented results are purely theoretical, all material parameters and geometries were chosen such that an experimental implementation should be feasible. Furthermore, we hypothesize the existence of configurations that allow for frequency absorption at points between simple parallel alignment or perfect checkerboard arrangements. If achievable, integrating this functional-

ity with chirped IDTs, which are capable of exciting a broad range of frequencies rather than a single one [52], would facilitate the development of a millimeter-sized RF notch filter with arbitrary frequency selectivity.

III. DISCUSSION

In this study, we have demonstrated the theoretical viability of a magneto-phononic device concept capable of switching SAW attenuation at a target frequency solely depending on its internal magnetic configuration. The shift in the SW dispersion relation resulting from the stray-field interactions of the parallel vs antiparallel aligned magnetic Co/Ni islets making up the device was shown to be significant enough to alter the SAW attenuation by as much as 28.9 dB/mm between them.

The algorithm developed to carry out these simulations was successfully validated on the results presented in ref. [21], showing that the assumptions made in its derivation are reasonable. Furthermore, due to the reduction in computational complexity by this approach, it is possible to sweep through a very large set of simulation parameters in a reasonable amount of time while maintaining great accuracy.

IV. METHODS

A. Uni-Directional Model: Derivation

The principal assumptions of the model are:

- The SAW only loses energy through a reduction in its amplitude A . Its velocity and mode are assumed to be constant and have to be known from simulations or analytical solutions. The simulation geometry then has to be chosen to be an integer multiple of the wavelength of that mode in the direction of travel.
- Measurements are only taken, once the system is in a state of constant energy flow between the mechanical and magnetic systems ($\frac{dR_T}{dt} = 0$). This can only occur for a sustained SAW signal of at least a couple periods (see Fig. 5).

We start by examining the total change in energy of the magnetic system $\frac{dE_M}{dt}$:

$$\frac{dE_M}{dt} = \int_{\Omega} \frac{d}{dt} U_M(t, \mathbf{m}(t)) d\mathbf{x} \quad (22)$$

$$= \underbrace{\int_{\Omega} \frac{\delta U_M(t, \mathbf{m}(t))}{\delta \mathbf{m}} \frac{d\mathbf{m}}{dt} d\mathbf{x}}_{\equiv R_L} + \underbrace{\int_{\Omega} \frac{\partial U_M(t, \mathbf{m}(t))}{\partial t} d\mathbf{x}}_{\equiv R_T}. \quad (23)$$

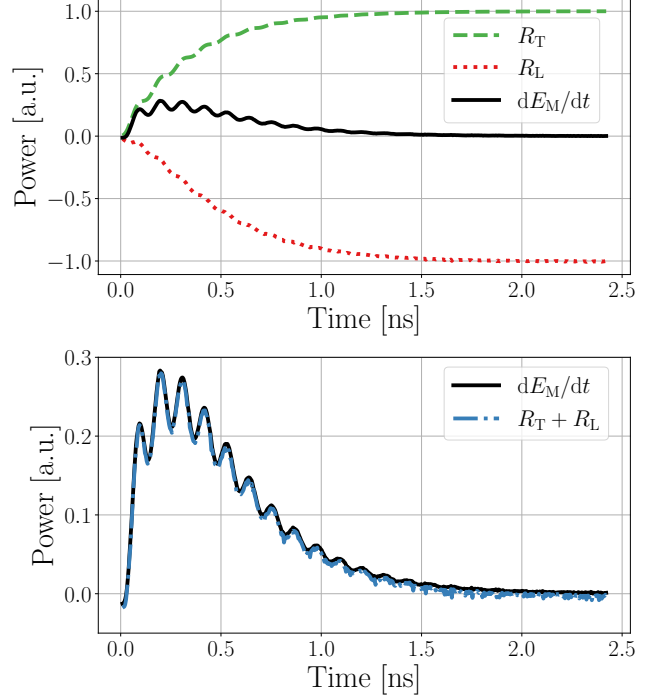


FIG. 5: Example simulation of the magneto-phononic interaction within a thin magnetic film under influence of an external field. The system was in energetic equilibrium when at $t = 0$ a continuous SAW signal was launched. The top graph shows the dissipative losses of the magnetic system (Eq. 24) in red, the energy transferred from the phonon to the magnon (Eq. 25) in green and the total change in energy in black (approximated via $\frac{dE_M}{dt}(t) \approx \frac{E_M(t+\Delta t) - E_M(t-\Delta t)}{2\Delta t}$). At $t = 2.43$ ns, the convergence criterion was reached. The bottom graph shows the validity of Eq. (23) with $R_T + R_L$ (blue) indeed summing to $\frac{dE_M}{dt}$ (black).

Here, U_M denotes the magnetic energy density and R_L are the dissipative losses due to Gilbert damping with the well known result [25]

$$R_L = -\frac{\alpha\gamma}{1+\alpha^2}\mu_0 M_s \int_{\Omega} (\mathbf{m} \times \mathbf{H}_{\text{Eff}})^2 d\mathbf{x}. \quad (24)$$

For R_T , we make use of the fact that, for constant H_{ext} , the magneto-elastic energy term (Eq. 2) is the only one that explicitly depends on time in E_M . When the simulation geometry is an integer multiple of the wavelength, $\int_{\Omega} \frac{\partial}{\partial t} (\boldsymbol{\varepsilon} : C : \boldsymbol{\varepsilon}) d\mathbf{x} = 0$. Given that $\boldsymbol{\varepsilon}_m$ has no explicit time dependence, $\frac{\partial \boldsymbol{\varepsilon}_m}{\partial t} = 0$. Thus, for a symmetric C , R_T simplifies to

$$R_T = - \int_{\Omega} \left(\frac{\partial \boldsymbol{\varepsilon}}{\partial t} \right) : C : \boldsymbol{\varepsilon}_m d\mathbf{x}. \quad (25)$$

Using the law of energy conservation, we know that all

energy gained by the magnetic system has to be compensated by a loss in the energy of the phonon, E_{Ph} :

$$\frac{dE_{\text{Ph}}}{dt} = -R_T = \int_{\Omega} \left(\frac{\partial}{\partial t} \boldsymbol{\varepsilon} \right) : C : \boldsymbol{\varepsilon}_m d\mathbf{x}. \quad (26)$$

If the magneto-phononic interaction is weak enough, that the LLG stays in a linear regime, it is known, that E_{Ph} follows an exponential decay [16, 21] (in the appendix, a possible extension of this approach to the non-linear regime is discussed):

$$E_{\text{Ph}}(t) = E_{\text{Ph}}(0)e^{\beta t}. \quad (27)$$

Using Eq. 26, we can express the decay rate β as

$$\beta = \beta \frac{E_{\text{Ph}}(0)e^{\beta t}}{E_{\text{Ph}}(0)e^{\beta t}} = \frac{1}{E_{\text{Ph}}(t)} \frac{dE_{\text{Ph}}}{dt}(t) = \frac{-R_T(t)}{E_{\text{Ph}}(t)} \quad (28)$$

where we can see, that it is sufficient to know R_T and E_{Ph} for any single point in time, in order to obtain β for the full interaction. R_T can be calculated from Eq. 25, where we simulate a segment of the magnetic material until R_T becomes constant (see fig 5). E_{Ph} can be obtained in a pre-simulation step by summing the potential energy $\frac{1}{2}\boldsymbol{\varepsilon} : C : \boldsymbol{\varepsilon}$ and kinetic energy $\frac{\rho\mathbf{v}^2}{2}$ of the SAW over the full volume V , including possible non-magnetic layers [49]:

$$E_{\text{Ph}} = \frac{1}{2} \int_V \boldsymbol{\varepsilon} : C : \boldsymbol{\varepsilon} + \rho\mathbf{v}^2 d\mathbf{x}. \quad (29)$$

Given that both $\boldsymbol{\varepsilon}$ and \mathbf{v} are derived from \mathbf{u} , they are proportional to A and therefore: $E_{\text{Ph}} \propto A^2$. Using $P \propto A^2$ [53], where P is the power of the SAW, we find:

$$P \propto E_{\text{Ph}}. \quad (30)$$

Finally, by viewing the phonon as a quasi-particle with a position $x(t) = ct$, where $c = v_t \xi$ is its velocity, we can give its energy in terms of its position instead of time:

$$E_{\text{Ph}}(t) = E_{\text{Ph}} \left(\frac{x(t)}{c} \right). \quad (31)$$

Combining Eq. 26 to 31, we obtain the magnetic transmission losses ΔS_{ij} by setting the position of the phonon $x(t)$ to the length of the magnetic material l :

$$\Delta S_{ij}(l) = 10 \log_{10} \left(\frac{P_{\text{out}}}{P_{\text{in}}} \right) \quad (32)$$

$$= 10 \log_{10} \left(\frac{E_{\text{Ph}}(l/c)}{E_{\text{Ph}}(0)} \right) \quad (33)$$

$$= 10 \log_{10} \left(\exp \left(\frac{l}{c} \beta \right) \right) \quad (34)$$

$$= \frac{10}{\ln(10)} \frac{l}{c} \beta \quad (35)$$

$$= \frac{10}{\ln(10)} \frac{l}{c} \frac{-R_T}{E_{\text{Ph}}} \quad (36)$$

$$= \frac{10}{\ln(10)} \frac{l}{c} \frac{\int_{\Omega} \left(\frac{\partial}{\partial t} \boldsymbol{\varepsilon} \right) : C : \boldsymbol{\varepsilon}_m d\mathbf{x}}{\frac{1}{2} \int_V \boldsymbol{\varepsilon} : C : \boldsymbol{\varepsilon} + \rho\mathbf{v}^2 d\mathbf{x}}. \quad (37)$$

B. Uni-Directional Model: Validation

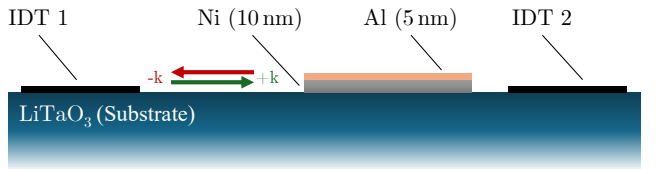


FIG. 6: Illustrated cross-section of the device employed in ref. [21]. On top of a 36°-rotated Y-cut X-propagation LiTaO_3 substrate, two inter digital transducers (IDTs) are placed 1600 μm apart. Between them, a 1000 μm long and 10 nm thick Ni film is applied and capped with a 5 nm Al layer. $+k$ and $-k$ indicate the direction of SAW travel.

To validate the model, we utilize material parameters from ref. [21], derived from both experimental measurements and fitting procedures. These parameters characterize a layered system comprising a 10 nm Ni thin film deposited on a LiTaO_3 substrate, capped with a 5 nm Al layer (see Fig. 6). We then compare the simulated transmission losses of a Rayleigh SAW with corresponding experimental results. The validation procedure is largely identical to the one introduced in sec. II F, only now the frequency of the SAW gets fixed at $f_{\text{SAW}} = 4.47 \text{ GHz}$, while the external field is varied. The following energy terms were considered: (i) demagnetization energy, (ii) exchange energy with stiffness A_{ex} , (iii) in-plane uniaxial magnetic anisotropy K_u^{IP} in easy axis direction ϕ_u^{IP} , (iv) OOP surface magnetic anisotropy counteracting the shape anisotropy K_u^{OOP} , (v) magneto-elastic energy with saturation magnetostriction λ_s , and (vi) Zeeman energy of an external field of strength H_{ext} and angle ϕ_H . ϕ_u^{IP} and ϕ_H are given in-plane with the x-axis. The SAW was again parameterized by the values from Tab. II. Mechanical parameters for Ni and Al are taken from ref. [21] and the magnetic parameters can be seen in Tab. III [21].

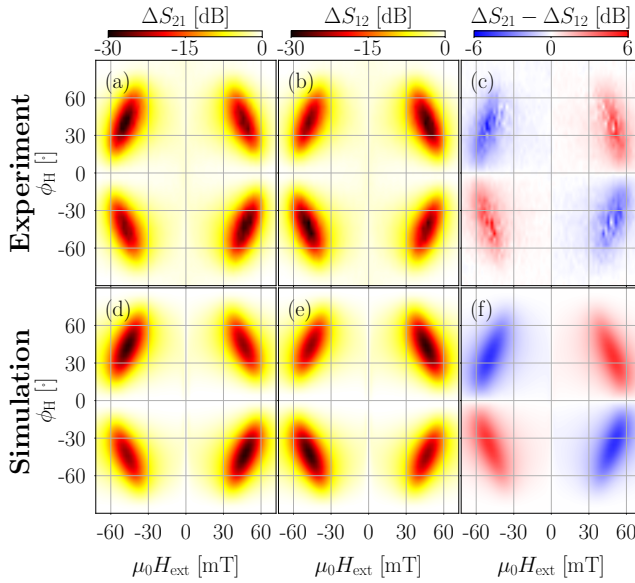


FIG. 7: (a) to (c): Experimental results of ref. [21]. (d) to (f): Results of micromagnetic simulations. (a), (b), (d), and (e) show the transmission losses due to the magneto-phononic interaction while (c) and (f) give the non-reciprocity between the travel directions.

TABLE III: Magnetic parameters of the 10 nm thick Ni film. [21]

α	M_s	A_{ex}	K_u^{IP}	ϕ_u^{IP}	K_u^{OOP}	λ_s
[1]	[kA/m]	[pJ/m]	[kJ/m ³]	[°]	[kJ/m ³]	[10 ⁻⁶]
0.069	408.0	7.7	0.28	83.6	23.8	-18.39

Here, K_u^{OOP} was fitted, such that the peak absorption for $\phi_H = 45^\circ$ occurs at the same $\mu_0 H_{ext}$ as the experiment (-46 mT). λ_s was then determined by matching simula-

tion results for ΔS_{21} ($\mu_0 H_{ext} = -46$ mT, $\phi_H = 45^\circ$) with the experimental value. This was done, because λ_s was not a fit parameter in ref. [21] and K_u^{OOP} was fitted in conjunction with an analytical approximation of the stray field in ref. [21], whereas the micromagnetic energy term given in Eq. (5) is used for the simulations here. Note that the fitted K_u^{OOP} of 23.8 kJ/m³ shows good agreement with the measured K_u^{OOP} of 32.7 kJ/m³ obtained from broadband ferromagnetic resonance measurements [21].

During validation, $\mu_0 H_{ext}$ was varied from -72 mT to 72 mT in increments of 2 mT and ϕ_H from -90° to 90° in increments of 4.5° for both directions of travel of the SAW, for a total of 5986 individual simulations. For each, the system was initialized with $\mathbf{m}(\mathbf{x}) = (\text{sgn}(H_{ext})\cos(\phi_H), \text{sgn}(H_{ext})\sin(\phi_H), 0)$ and relaxed before the SAW was activated.

The results of this validation run can be seen in Fig. 7. The micromagnetic simulation and the experimental results show excellent agreement not only qualitatively but also quantitatively for both directions of SAW travel. The expected four-fold symmetry is clearly present, as well as the non-reciprocity between the two directions of travel. The validation took a total of ≈ 100 hours on an NVIDIA A100 (80GB) GPU, for an average of only ≈ 1 minute per simulation.

V. ACKNOWLEDGMENT

This work was funded in whole or in part by the Austrian Science Fund (FWF) [DOI: 10.55776/I6068] and by the Deutsche Forschungsgemeinschaft (DFG, German Research Foundation) project No. 504150161. For open access purposes, the author has applied a CC BY public copyright license to any author-accepted manuscript version arising from this submission.

-
- [1] D. Morgan, History of saw devices, in *Proceedings of the 1998 IEEE International Frequency Control Symposium (Cat. No.98CH36165)* (1998) pp. 439–460.
 - [2] D. Morgan, *Surface Acoustic Wave Filters: With Applications to Electronic Communications and Signal Processing*, Studies in Electrical and Electronic Engineering (Academic Press, 2010).
 - [3] C. Campbell, *Surface Acoustic Wave Devices and Their Signal Processing Applications* (Academic Press, 2012).
 - [4] R. M. White and F. W. Voltmer, Direct piezoelectric coupling to surface elastic waves, *Applied Physics Letters* **7**, 10.1063/1.1754276 (1965).
 - [5] C. Ruppel, L. Reindl, and R. Weigel, Saw devices and their wireless communications applications, *IEEE Microwave Magazine* **3**, 65 (2002).
 - [6] P. Chen, G. Li, and Z. Zhu, Development and application of saw filter (2022).
 - [7] P. Delsing, A. N. Cleland, M. J. Schuetz, J. Knörzer, G. Giedke, J. I. Cirac, K. Srinivasan, M. Wu, K. C. Balram, C. Baüerle, T. Meunier, C. J. Ford, P. V. Santos, E. Cerdá-Méndez, H. Wang, H. J. Krenner, E. D. Nyffenegger, M. Weiß, G. R. Nash, L. Thevenard, C. Gourdon, P. Rovillain, M. Marangolo, J. Y. Duquesne, G. Fischerauer, W. Ruile, A. Reiner, B. Paschke, D. Denysenko, D. Volkmer, A. Wixforth, H. Bruus, M. Wiklund, J. Reboud, J. M. Cooper, Y. Q. Fu, M. S. Brugger, F. Rehfeldt, and C. Westerhausen, The 2019 surface acoustic waves roadmap, *Journal of Physics D: Applied Physics* **52**, 10.1088/1361-6463/ab1b04 (2019).
 - [8] D. Mandal and S. Banerjee, Surface acousticwave (saw) sensors: Physics, materials, and applications, *Sensors* **22**, 10.3390/s22030820 (2022).
 - [9] X. Ding, S. C. S. Lin, B. Kiraly, H. Yue, S. Li, I. K. Chiang, J. Shi, S. J. Benkovic, and T. J. Huang, On-chip manipulation of single microparticles, cells, and or-

- ganisms using surface acoustic waves, *Proceedings of the National Academy of Sciences of the United States of America* **109**, 10.1073/pnas.1209288109 (2012).
- [10] J. Rufo, F. Cai, J. Friend, M. Wiklund, and T. J. Huang, Acoustofluidics for biomedical applications, *Nature Reviews Methods Primers* **2**, 10.1038/s43586-022-00109-7 (2022).
- [11] B. Luo, P. Velvaluri, Y. Liu, and N.-X. Sun, Magneto-electric baw and saw devices: A review, *Micromachines* **15**, 10.3390/mi15121471 (2024).
- [12] D. A. Bozhko, V. I. Vasyuchka, A. V. Chumak, and A. A. Serga, Magnon-phonon interactions in magnon spintronics (review article), *Low Temperature Physics* **46**, 10.1063/10.0000872 (2020).
- [13] W. G. Yang and H. Schmidt, Acoustic control of magnetism toward energy-efficient applications, *Applied Physics Reviews* **8**, 10.1063/5.0042138 (2021).
- [14] J. Puebla, Y. Hwang, S. Maekawa, and Y. Otani, Perspectives on spintronics with surface acoustic waves, *Applied Physics Letters* **120**, 10.1063/5.0093654 (2022).
- [15] M. Weiler, L. Dreher, C. Heeg, H. Huebl, R. Gross, M. S. Brandt, and S. T. Goennenwein, Elastically driven ferromagnetic resonance in nickel thin films, *Physical Review Letters* **106**, 10.1103/PhysRevLett.106.117601 (2011).
- [16] L. Dreher, M. Weiler, M. Pernpeintner, H. Huebl, R. Gross, M. S. Brandt, and S. T. Goennenwein, Surface acoustic wave driven ferromagnetic resonance in nickel thin films: Theory and experiment, *Physical Review B - Condensed Matter and Materials Physics* **86**, 10.1103/PhysRevB.86.134415 (2012).
- [17] X. Li, D. Labanowski, S. Salahuddin, and C. S. Lynch, Spin wave generation by surface acoustic waves, *Journal of Applied Physics* **122**, 10.1063/1.4996102 (2017).
- [18] B. Casals, N. Statuto, M. Foerster, A. Hernández-Mínguez, R. Cicheler, P. Manshausen, A. Mandziak, L. Aballe, J. M. Hernández, and F. Macià, Generation and imaging of magnetoacoustic waves over millimeter distances, *Phys. Rev. Lett.* **124**, 137202 (2020).
- [19] Y. Kunz, M. Küß, M. Schneider, M. Geilen, P. Pirro, M. Albrecht, and M. Weiler, Coherent surface acoustic wave–spin wave interactions detected by micro-focused brillouin light scattering spectroscopy, *Applied Physics Letters* **124**, 152403 (2024).
- [20] K. Yamamoto, M. Xu, J. Puebla, Y. Otani, and S. Maekawa, Interaction between surface acoustic waves and spin waves in a ferromagnetic thin film, *Journal of Magnetism and Magnetic Materials* **545**, 168672 (2022).
- [21] M. Küß, M. Heigl, L. Flacke, A. Hefele, A. Hörner, M. Weiler, M. Albrecht, and A. Wixforth, Symmetry of the magnetoelastic interaction of rayleigh and shear horizontal magnetoacoustic waves in nickel thin films on ltao3, *Physical Review Applied* **15**, 10.1103/PhysRevApplied.15.034046 (2021).
- [22] D. A. Bas, R. Verba, P. J. Shah, S. Leontsev, A. Matyushov, M. J. Newburger, N. X. Sun, V. Tyberkevich, A. Slavin, and M. R. Page, Nonreciprocity of phase accumulation and propagation losses of surface acoustic waves in hybrid magnetoelastic heterostructures, *Phys. Rev. Appl.* **18**, 044003 (2022).
- [23] E. M. Lifshitz and L. D. Landau, On the theory of dispersion of magnetic permeability in ferromagnetic bodies, *Phys. Zeitsch. der Sow.* **8** (1935).
- [24] T. L. Gilbert, A lagrangian formulation of the gyromagnetic equation of the magnetic field, *Phys. Rev.* **100** (1955).
- [25] C. Abert, Micromagnetics and spintronics: models and numerical methods, *European Physical Journal B* **92**, 10.1140/epjb/e2019-90599-6 (2019).
- [26] Y. C. Shu, M. P. Lin, and K. C. Wu, Micromagnetic modeling of magnetostrictive materials under intrinsic stress, *Mechanics of Materials* **36**, 10.1016/j.mechmat.2003.04.004 (2004).
- [27] J. X. Zhang and L. Q. Chen, Phase-field microelasticity theory and micromagnetic simulations of domain structures in giant magnetostrictive materials, *Acta Materialia* **53**, 10.1016/j.actamat.2005.03.002 (2005).
- [28] S. Chikazumi and C. Graham, *Physics of Ferromagnetism 2e*, International Series of Monographs on Physics (OUP Oxford, 2009).
- [29] C. Y. Liang, S. M. Keller, A. E. Sepulveda, A. Bur, W. Y. Sun, K. Wetzel, and G. P. Carman, Modeling of magnetoelastic nanostructures with a fully coupled mechanical-micromagnetic model, *Nanotechnology* **25**, 10.1088/0957-4484/25/43/435701 (2014).
- [30] F. Vanderveken, J. Mulders, J. Leliaert, B. V. Waeyenberge, B. Sorée, O. Zografos, F. Ciubotaru, and C. Adelmann, Finite difference magnetoelastic simulator, *Open Research Europe* **1**, 10.12688/openreseurope.13302.1 (2021).
- [31] M. Küß, M. Heigl, L. Flacke, A. Hörner, M. Weiler, M. Albrecht, and A. Wixforth, Nonreciprocal dzyaloshinskii-moriya magnetoacoustic waves, *Physical Review Letters* **125**, 10.1103/PhysRevLett.125.217203 (2020).
- [32] F. Bruckner, S. Koraltan, C. Abert, and D. Suess, magnum.np: a pytorch based gpu enhanced finite difference micromagnetic simulation framework for high level development and inverse design, *Scientific Reports* **13**, 10.1038/s41598-023-39192-5 (2023).
- [33] L. You, R. C. Sousa, S. Bandiera, B. Rodmacq, and B. Dieny, Co/ni multilayers with perpendicular anisotropy for spintronic device applications, *Applied Physics Letters* **100**, 10.1063/1.4704184 (2012).
- [34] X. D. He, L. L. Zhang, G. J. Wu, J. W. Gao, P. Ran, M. Sajjad, X. W. Zhou, J. W. Cao, L. Xi, Y. L. Zuo, and Y. Ren, Controllable intrinsic gilbert damping in pt buffered [co/ni]_n multilayers with enhanced perpendicular magnetic anisotropy, *Journal of Magnetism and Magnetic Materials* **519**, 10.1016/j.jmmm.2020.167429 (2021).
- [35] S. Mizukami, X. Zhang, T. Kubota, H. Naganuma, M. Oogane, Y. Ando, and T. Miyazaki, Gilbert damping in ni/co multilayer films exhibiting large perpendicular anisotropy, *Applied Physics Express* **4**, 10.1143/APEX.4.013005 (2011).
- [36] D. B. Gopman, P. Chen, J. W. Lau, A. C. Chavez, G. P. Carman, P. Finkel, M. Staruch, and R. D. Shull, Large Interfacial Magnetostriction in (Co/Ni)₄/Pb(Mg_{1/3}Nb_{2/3})O₃-PbTiO₃ Multiferroic Heterostructures, *ACS Applied Materials and Interfaces* **10**, 10.1021/acsami.8b06249 (2018).
- [37] E. Klokhholm and J. Aboaf, The saturation magnetostriction of thin polycrystalline films of iron, cobalt, and nickel, *Journal of Applied Physics* **53**, 10.1063/1.330930 (1982).
- [38] K. E. Kim and C. H. Yang, Local magnetostriction measurement in a cobalt thin film using scanning probe microscopy, *AIP Advances* **8**, 10.1063/1.5043466 (2018).

- [39] T. M. Project, Materials Data on Co by Materials Project 10.17188/1186809 (2020).
- [40] T. M. Project, Materials Data on Ni by Materials Project 10.17188/1199153 (2020).
- [41] A. Jain, S. P. Ong, G. Hautier, W. Chen, W. D. Richards, S. Dacek, S. Cholia, D. Gunter, D. Skinner, G. Ceder, and K. A. Persson, Commentary: The materials project: A materials genome approach to accelerating materials innovation, *APL Materials* **1**, 10.1063/1.4812323 (2013).
- [42] T. M. Project, Materials Data on Ta by Materials Project 10.17188/1208553 (2020).
- [43] T. M. Project, Materials Data on Pt by Materials Project 10.17188/1189002 (2020).
- [44] G. Venkat, D. Kumar, M. Franchin, O. Dmytriev, M. Mruczkiewicz, H. Fangohr, A. Barman, M. Krawczyk, and A. Prabhakar, Proposal for a standard micromagnetic problem: Spin wave dispersion in a magnonic waveguide, *IEEE Transactions on Magnetics* **49**, 10.1109/TMAG.2012.2206820 (2013).
- [45] M. Krawczyk and D. Grundler, Review and prospects of magnonic crystals and devices with reprogrammable band structure, *Journal of Physics Condensed Matter* **26**, 10.1088/0953-8984/26/12/123202 (2014).
- [46] K. Nakamura, M. Kazumi, and H. Shimizu, SH-Type and Rayleigh-Type Surface Waves on Rotated Y-Cut LiTaO₃, in *1977 Ultrasonics Symposium* (1977) pp. 819–822.
- [47] M. M. Sonner, F. Khosravi, L. Janker, D. Rudolph, G. Koblmüller, Z. Jacob, and H. J. Krenner, Ultrafast electron cycloids driven by the transverse spin of a surface acoustic wave, *Science Advances* **7**, 10.1126/sci-adv.abf7414 (2021).
- [48] S. Maekawa and M. Tachiki, Surface acoustic attenuation due to surface spin wave in ferro- and antiferromagnets, *AIP Conference Proceedings* **29**, 542 (1976).
- [49] L. D. Landau, E. M. Lifshitz, J. B. Sykes, W. H. Reid, and E. H. Dill, Theory of elasticity: Vol. 7 of course of theoretical physics, *Physics Today* **13**, 10.1063/1.3057037 (1960).
- [50] COMSOL, COMSOL Multiphysics® v. 6.2.0.339, www.comsol.com, COMSOL AB, Stockholm, Sweden.
- [51] T. M. Project, Materials Data on LiTaO₃ by Materials Project 10.17188/1207210 (2020).
- [52] M. Weiß, A. L. Hörner, E. Zallo, P. Atkinson, A. Rastelli, O. G. Schmidt, A. Wixforth, and H. J. Krenner, Multiharmonic frequency-chirped transducers for surface-acoustic-wave optomechanics, *Phys. Rev. Appl.* **9**, 014004 (2018).
- [53] W. P. Robbins, A simple method of approximating surface acoustic wave power densities, *IEEE Transactions on Sonics and Ultrasonics* **24**, 10.1109/T-SU.1977.30956 (1977).

Appendix A: Uni-Directional Model: Extension to non-linear excitations

The uni-directional model could be extended to non-linear regions of the LLG, where the exponential ansatz no longer holds, by introducing an iterative approach: Starting from a specific amplitude A_0 one calculates the starting energy of the phonon $E_{\text{Ph}, 0}$, simulates until condition $\frac{dR_T}{dt} = 0$ is reached and determines $\frac{dE_{\text{Ph}}}{dt}$. With

this information, one can then calculate the amplitude A_1 the phonon has a small distance $\Delta l = c\Delta t$ away by making use of a first order Taylor approximation and $E_{\text{Ph}} \propto A^2$:

$$\frac{E_{\text{Ph}, n+1}}{E_{\text{Ph}, 0}} = \frac{A_{n+1}^2}{A_0^2} \quad (\text{A1})$$

$$\Rightarrow A_{n+1} = A_0 \sqrt{\frac{E_{\text{Ph}, n+1}}{E_{\text{Ph}, 0}}} \quad (\text{A2})$$

$$= A_0 \sqrt{\frac{E_{\text{Ph}, n} + \Delta t \frac{dE_{\text{Ph}, n}}{dt}}{E_{\text{Ph}, 0}}} \quad (\text{A3})$$

$$= A_0 \sqrt{\frac{E_{\text{Ph}, n}}{E_{\text{Ph}, 0}} + \frac{\frac{\Delta l}{c} \frac{dE_{\text{Ph}, n}}{dt}}{E_{\text{Ph}, 0}}} \quad (\text{A4})$$

$$= A_0 \sqrt{\frac{A_n^2}{A_0^2} + \frac{\Delta l}{c \cdot E_{\text{Ph}, 0}} \int_{\Omega} \left(\frac{\partial}{\partial t} \boldsymbol{\varepsilon} \right) : \boldsymbol{\varepsilon}_m d\mathbf{x}}. \quad (\text{A5})$$

Repeating this process of determining $\frac{dE_{\text{Ph}}}{dt}$ with the new amplitude and then readjusting it, N times, one arrives at the transmission losses ΔS_{ij} after the distance $l = N\Delta l$:

$$\Delta S_{ij}(l) = 10 \log_{10} \left(\frac{P_{\text{out}}}{P_{\text{in}}} \right) \quad (\text{A6})$$

$$= 10 \log_{10} \left(\frac{A_N^2}{A_0^2} \right). \quad (\text{A7})$$

In cases where the exponential ansatz does hold, so if $\frac{dE_{\text{Ph}, n}}{dt} = \beta E_{\text{Ph}, n} \forall n$ with $\beta = \text{const.}$, then this iterative algorithm is equivalent to the regular uni-directional model for infinitesimal Δl :

$$\frac{A_N^2}{A_0^2} = \frac{E_{\text{Ph}, N}}{E_{\text{Ph}, 0}} \quad (\text{A8})$$

$$= \frac{E_{\text{Ph}, N-1} + \Delta t \frac{dE_{\text{Ph}, N-1}}{dt}}{E_{\text{Ph}, 0}} \quad (\text{A9})$$

$$= \frac{E_{\text{Ph}, N-1} + \frac{\Delta l}{c} \beta E_{\text{Ph}, N-1}}{E_{\text{Ph}, 0}} \quad (\text{A10})$$

$$= \frac{(1 + \frac{\Delta l}{c} \beta) E_{\text{Ph}, N-1}}{E_{\text{Ph}, 0}} \quad (\text{A11})$$

$$= \frac{(1 + \frac{\Delta l}{c} \beta) (E_{\text{Ph}, N-2} + \frac{\Delta l}{c} \beta E_{\text{Ph}, N-2})}{E_{\text{Ph}, 0}} \quad (\text{A12})$$

$$= \frac{(1 + \frac{\Delta l}{c} \beta)^2 E_{\text{Ph}, N-2}}{E_{\text{Ph}, 0}} \quad (\text{A13})$$

⋮

$$= \frac{(1 + \frac{\Delta l}{c} \beta)^N E_{\text{Ph}, N-N}}{E_{\text{Ph}, 0}} \quad (\text{A14})$$

$$= \left(1 + \frac{\Delta l}{c} \beta\right)^N \quad (\text{A15})$$

$$= \left(1 + \frac{\Delta l}{c} \beta\right)^{\frac{l}{\Delta l}} \quad (\text{A16})$$

$$= \left(\left(1 + \frac{\Delta l}{c} \beta\right)^{\frac{1}{\Delta l}}\right)^l \quad (\text{A17})$$

$$\Rightarrow \lim_{\Delta l \rightarrow 0} \frac{A_N^2}{A_0^2} = \lim_{\Delta l \rightarrow 0} \left(\left(1 + \frac{\Delta l}{c} \beta\right)^{\frac{1}{\Delta l}}\right)^l \quad (\text{A18})$$

$$= \left(\lim_{\Delta l \rightarrow 0} \left(1 + \frac{\Delta l}{c} \beta\right)^{\frac{1}{\Delta l}}\right)^l \quad (\text{A19})$$

$$= \left(\exp\left(\frac{1}{c}\beta\right)\right)^l \quad (\text{A20})$$

$$= \exp\left(\frac{l}{c}\beta\right) \quad (\text{A21})$$

$$\Rightarrow 10\log_{10}\left(\frac{A_N^2}{A_0^2}\right) = 10\log_{10}\left(\exp\left(\frac{l}{c}\beta\right)\right). \quad (\text{A22})$$